

RESEARCH

Open Access



Influence of extreme fracture flow channels on the thermal performance of open-loop geothermal systems at commercial scale

Nicolás Rangel-Jurado^{1,2}, Adam J. Hawkins¹ and Patrick M. Fulton^{1*} 

*Correspondence:
pfulton@cornell.edu

¹ Cornell University, Ithaca, NY, USA

² Present Address: ETH Zurich, Zurich, Switzerland

Abstract

Adequate stewardship of geothermal resources requires accurate forecasting of long-term thermal performance. In enhanced geothermal systems and other fracture-dominated reservoirs, predictive models commonly assume constant-aperture fractures, although spatial variations in aperture can greatly affect reservoir permeability, fluid flow distribution, and heat transport. Whereas previous authors have investigated the effects of theoretical random aperture distributions on thermal performance, here we further explore the influence of permeability heterogeneity considering field-constrained aperture distributions from a meso-scale field site in northern New York, USA. Using numerical models of coupled fluid flow and heat transport, we conduct thermal–hydraulic simulations for a hypothetical reservoir consisting of a relatively impervious porous matrix and a single, horizontal fracture. Our results indicate that in highly channelized fields, most well design configurations and operating conditions result in extreme rates of thermal drawdown (e.g., 50% drop in production well temperatures in under 2 years). However, some other scenarios that account for the risks of short-circuiting can potentially enhance heat extraction when mass flow rate is not excessively high, and the direction of geothermal extraction is not aligned with the most permeable features in the reservoir. Through a parametric approach, we illustrate that well separation distance and relative positioning play a major role in the long-term performance of highly channelized fields, and both can be used to help mitigate premature thermal breakthrough.

Keywords: Thermal performance, Fluid flow short-circuiting, Enhanced geothermal systems, Reservoir management strategies

Introduction

Geothermal energy has the potential to provide carbon-free, baseload and renewable energy for several generations to come. However, uncertainty in forecasting the commercial lifetime of a site-specific geothermal system remains a considerable barrier to attracting investment capital (e.g., Watanabe et al. 2010; Pandey and Vishal 2017). Among other technical challenges for geothermal energy, thermal interference between cold injectors and hot producers, or “short-circuiting”, can result in substantial drops in production temperature that endangers the reservoir’s long-term commercial success

(Tsang and Neretnieks 1997; Kolditz and Clauser 1998; Hui et al. 2018). This concern is particularly true in Enhanced Geothermal Systems (EGS) as fluid flow is expected to concentrate in fractures and other narrow flow channels that reduce the effective inter-well surface area available for heat transfer (Murphy et al. 1981; Brown 1987; Lu 2018). Existing literature addressing this issue has determined the range of uncertainties for a single discrete rock fracture with non-uniform fracture aperture (e.g., Fox et al. 2015; Ghassemi et al. 2005; Guo et al. 2016). However, the statistical descriptions of the aperture variability largely reflect small-scale (cm) measurements on rock core, which in most cases fail to represent a reasonable representative elementary volume for large-scale reservoirs (Corbett et al. 1998; Farmer 2002). Alternatively, Neuville et al. (2010), Fox et al. (2015), and Guo et al. (2016) evaluate the influence of fluid flow short circuits on the thermal behavior of single-fracture geothermal reservoirs using randomly generated, self-affine or auto-correlated, aperture fields. The sparsity and limited accessibility of *real* permeability datasets represent considerable obstacles when transitioning from theoretical investigations to the development of site-specific predictive models.

Another challenge for these types of studies has been the presumption that the spatial heterogeneity of a fracture flow system cannot be well characterized a priori or even once wells are drilled and tested. Thus, interpretations of results are often limited in the practical operational strategies that can be employed to optimize thermal performance. However, recent advances in fracture seismic imaging, analysis of inert and active tracers along with other hydrologic and geophysical observables are beginning to illustrate the potential for characterizing subsurface flow systems and the spatial distribution of hydraulic fracture aperture or permeability along large-scale fracture systems (e.g., Sickling and Malin 2019; Pyrak-Nolte et al. 2020; Hawkins et al. 2020; Zhao et al. 2021).

Here, we utilize a rare and interesting dataset of fracture aperture variations characterized at a meso-scale (~ 14 m) field site (Hawkins et al. 2020). The data exhibit extreme channelization, beyond what has been evaluated for in commercial-scale geothermal modeling in the past. Thus, we return to the heterogenous fracture flow problem to evaluate the effects such an extreme scenario would have on the thermal production of a geothermal well pair if upscaled to commercial scale (100's of meters) and consider the influence of different operating conditions and well placement strategies with the understanding that the nature of preferential flow channels may indeed be characterizable.

The objective of this study is therefore to assess at the geothermal commercial scale, the implications of extreme flow channeling, as seen in nature, and develop potential reservoir management strategies to mitigate resource deterioration resulting from thermal drawdown induced by fluid flow short-circuiting.

For this work, we use a previously published, field-derived fracture aperture distribution which describes a meso-scale fracture that exhibits extreme flow channeling (Hawkins et al. 2020). This highly conductive fracture is a research focus of the Altona Field Laboratory (i.e., "Altona"), which is located ~ 6 km northwest of West Chazy, New York in northeastern New York state near the borders with Canada and Vermont (Fig. 1). The fracture is oriented sub-horizontally at a depth of roughly 7.6 m below ground surface and is intersected by five separate wells within a 10×10 m square. This site is well-characterized hydraulically and geophysically, and has been extensively used for studying fracture-dominated fluid flow, heat transfer, and chemical

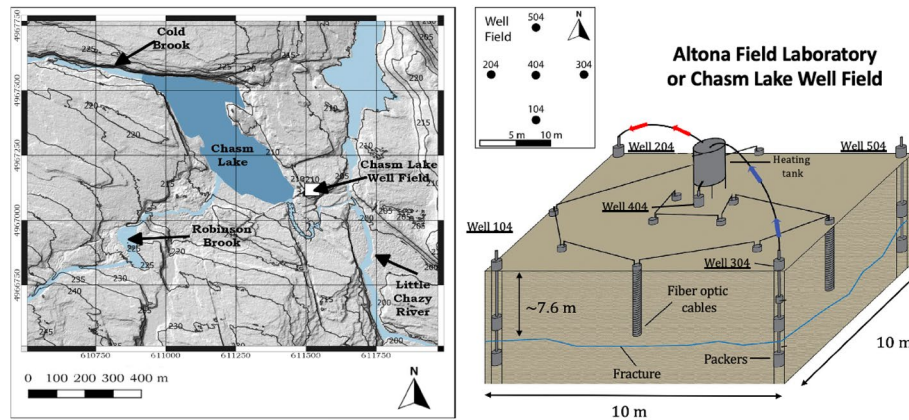


Fig. 1 On the left, a Digital Elevation Map (DEM) of the region surrounding the Altona Field Laboratory in upstate New York, USA. White rectangle represents the approximate location of the five-spot well field (Taken and modified from Hawkins 2017). On the right-hand side, a three-dimensional schematic of Altona shows the 5-well configuration. Red and blue arrows depict the circulation of fluids being injected into the reservoir at high temperatures and being pumped back to the surface to be heated through a tankless water heater and re-injected again (Adapted after Hawkins 2017)

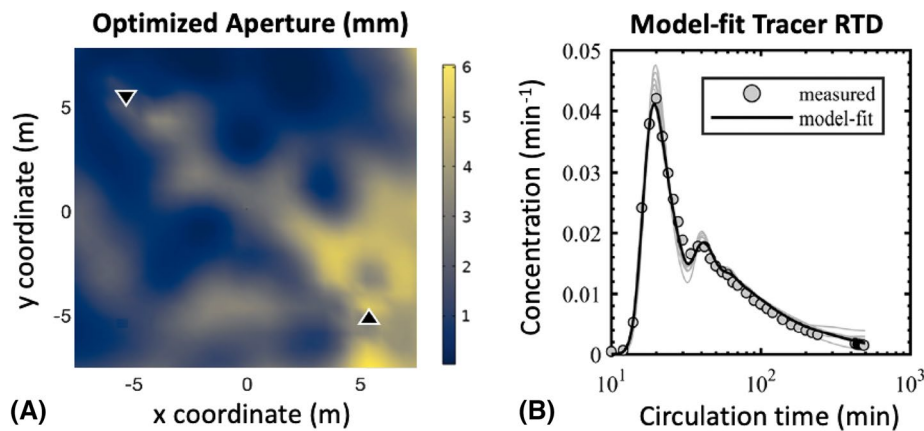


Fig. 2 **A:** Best fit aperture distribution calibrated by frictional pressure loss and an inert tracer test. Black triangles represent the location of the injection and production wells. **B:** Measured and simulated residence time distribution (RTD) curves for inert tracers throughout 6 days of fluid circulation. Note that lighter gray lines represent multiple repetitions of the machine learning algorithm, while the black line represents the repetition that provided the best agreement with field observations. Highlighted model fit in Panel **B** used the best-fit aperture distribution in Panel **A** as input. (Adapted from Hawkins et al. 2020)

transport processes (Hawkins et al. 2017a, 2017b, Hawkins et al. 2018, Hawkins et al. 2020). The geologic formation containing the fracture, the Cambrian-aged Potsdam Sandstone, is a well-cemented stratigraphic unit that has low porosity (~1%) but widespread and natural fractures, which makes the crystalline rock formation highly permeable at large scale (Rayburn et al. 2005; Olcott 1995).

The fracture aperture distribution for this fracture (Fig. 2A) results from a machine learning (genetic algorithm) inversion of pressure drop and tracer time-series data from an active dipole injection/production test (Hawkins et al. 2020). Figure 2B shows the measured and simulated tracer breakthrough curves for the inert tracer

test experiment during roughly 500 min of fluid circulation alongside the model fit conducted using the best-fit aperture distribution in Fig. 2A.

The optimized aperture distribution (Fig. 2A) is dependent on the wellbore layout and other operating conditions of the circulation experiment, conducted in 2015. As such, the optimized aperture distribution constitutes a virtual representation of field data, rather than the true fracture aperture at Altona. However, the general highly channelized nature of the fracture is also corroborated by observations of thermal and inert tracer breakthrough in alternative well-pair pumping scenarios, and ground-penetrating radar imaging of subsurface tracer transport (Hawkins et al. 2017a, b). It is the high level of real-world spatial characterization and extreme fluid flow channelization which make this dataset particularly useful as a basis for evaluating potential extreme scenarios in geothermal reservoirs.

Methods

To calculate how a real-world, large-scale, extremely channelized fracture aperture distribution can affect heat transfer processes in geothermal reservoirs, we employ a numerical model that simulates the thermal–hydraulic behavior of a single-fracture reservoir displaying a non-uniform permeability distribution. For this, we use COMSOL Multiphysics 5.6., which is a finite element method numerical software that solves partial differential equations of coupled multi-physical phenomena and is employed broadly in a variety of scientific and engineering settings (COMSOL 2019). Because COMSOL is a general modeling software that can solve a wide variety of different physics, we describe our approach and particular governing equations below. For instance, our 3D advection–diffusion reservoir model fully couples the heat transfer from the bulk rock, assuming 3D thermal conduction in the rock matrix while simultaneously solving the governing equations of fluid flow and heat transfer in the 2D fracture are based on the tangential derivatives along the internal boundary representing the fracture.

For naturally fractured reservoirs or enhanced geothermal systems (EGS), fluid flow and heat transport will preferentially occur along rock fractures since these are usually orders of magnitude more permeable than the bulk rock matrix (National Research Council 1996). The conservation of mass for a Newtonian fluid in a single-fracture reservoir is governed by the common equation:

$$b \frac{\partial}{\partial t} (\rho_w) + \nabla_T (b \rho_w u_f) = b Q_m \quad (1)$$

where t is transient time, ρ_w is the density of water or the circulating fluid, ∇_T indicates the gradient operator restricted to the fracture's tangential plane, u_f is the Darcy velocity of the fluid inside the fracture, and Q_m is the mass source term. Note that the velocity field adopted here is spatially variable in accordance with the aperture field and locations of sinks/sources, but is assumed to remain constant over time. The fracture, which can have a spatially-variable local aperture, is confined by no-flow boundaries in the x -direction meaning no mass flow is allowed through the spatial boundaries of the model domain. Hence, the reservoir is assumed to be hydraulically isolated from the surrounding formation.

The heat transfer in this system occurs both in the bulk rock matrix through conduction and in the fracture via forced advection. Thermal conduction in the bulk rock matrix is governed by the three-dimensional thermal diffusion equation as:

$$(\rho C_p)_{eff} \frac{\partial T}{\partial t} = -\rho_w C_{p,w} u \cdot \nabla T - \nabla \cdot (-k_{eff} \nabla T) + Q_{th} \tag{2}$$

where $(\rho C_p)_{eff}$ is the effective volumetric heat capacity for the bulk rock matrix, T is the temperature of the rock, ϕ_r is the rock porosity, k_{eff} the effective thermal conductivity of the bulk rock matrix, ρ_r and $C_{p,r}$ are the density and specific heat capacity of the rock, respectively, and Q_{th} is the heat flux term that corresponds to a position on the two-dimensional fracture plane. Moreover, the effective volumetric heat capacity is given by Eq. 3:

$$(\rho C_p)_{eff} = (1 - \phi_r) \rho_r C_{p,r} + \phi_r \rho_w C_{p,w} \tag{3}$$

The heat transfer equilibrium between the bulk rock matrix and the fracture is derived from the conservation of energy law and expressed as:

$$b (\rho C_p)_{eff,f} \frac{\partial T}{\partial t} = -b \rho_w C_{p,w} u_f \cdot \nabla T - \nabla_T \cdot (-b k_{eff,f} \nabla_T T) + b Q_{th,f} \tag{4}$$

where the subscript f corresponds to fracture properties. The heat source term in the fracture $Q_{th,f}$ is related to the rate of advection along the fracture surface and is coupled to the thermal conduction from the bulk rock matrix in Eq. 2. As a result, Eqs. 2, 4 are solved simultaneously to determine the surface heat flux between the fracture and the bulk rock matrix. Heat transfer between the rock and the fluid is assumed to be at local equilibrium, which means that the temperature of the fluid within the fracture aperture is in equilibrium with the fracture-matrix interface such that:

$$T(x, y, t) = T \tag{5}$$

where T is the temperature of both the rock and the fluid at time t in a given point in a 2D space.

Temperature is restricted by the initial and boundary conditions:

$$T(x, y, 0) = T_{res} \tag{6}$$

$$T(x_i, y_i, t) = T_{inj}, \quad t > 0 \tag{7}$$

Equation 6 implies that at time equal to zero, the rock and fracture fluids are at a constant initial reservoir temperature T_r , whereas Eq. 7 indicates that the injection point has a constant injection temperature T_{inj} for all times greater than zero where the fluid is being injected at a constant mass flow rate \dot{m} . As a result, the thermal output of the system $\dot{Q}(t)$ is the key variable of interest, varies over time and is defined as:

$$\dot{Q}(t) = \dot{m} C_{p,f} (T_{prod} - T_{inj}) \tag{8}$$

Fluid density and dynamic viscosity commonly vary as a function of both temperature and pressure. However, under the typical conditions of low-enthalpy geothermal reservoirs, the fluid properties of water are mainly dependent on temperature (Bundschuh and Suárez-Arriaga, 2010). As the temperature rises, water becomes less dense and less viscous. Our simulations consider the effect of temperature-dependent variations in density (ranging from ~ 920 to 1000 kg · m⁻³) and viscosity (ranging from 0.0018 to 0.002 Pa · s) based on the empirical approximations reported by Chandrasekharam and Bundschuh (2008) for temperatures between 0 and 150 °C as:

$$\rho(T) = \begin{cases} 1000.0 (1.0 - 8.0 \cdot 10^{-6} \cdot (T - 3.98)^2); & 0^\circ C \leq T \leq 20^\circ C \\ 996.9 \cdot (1.0 - 3.17 \cdot 10^{-4} \cdot (T - 25.0) - 2.56 \cdot 10^{-6} \cdot (T - 25.0)^2); & 20^\circ C \leq T \leq 150^\circ C \end{cases} \quad (9)$$

and

$$\mu(T) = \begin{cases} 10^{-3} (1.0 + 0.015512 (T - 20.0))^{-1.572}, & 0^\circ C \leq T \leq 100^\circ C \\ 241.4 \cdot 10^{-7} \cdot 10^{\frac{247.8}{T+133.15}}, & 100^\circ C \leq T \leq 150^\circ C \end{cases} \quad (10)$$

The range of pressure conditions modeled in this study ensures that water remains in the liquid state, thus, the effects of flashing are not considered.

Inside the fracture, we consider fluid flow to be laminar, which allows us to relate the effective permeability term in Eq. 4 to fracture aperture *b*. Laminar flow is governed by the Hele-Shaw equation, also known as the “cubic law” (Witherspoon et al. 1980; Zimmerman and Bodvarsson 1996):

$$Q = \frac{b^3 w \Delta P}{12 \mu L} \quad \text{s.t. } w \gg b \quad (11)$$

where *Q* is the volumetric flow rate, *b* is the fracture aperture, *w* is the fracture width, ΔP is the frictional pressure loss, μ is the dynamic viscosity of the fluid, and *L* is the length of the fracture channel. The use of this analytical solution assumes the fluid to be viscous and incompressible. Comparing Eq. 11 with Darcy’s Law,

$$u_f = - \frac{k}{\mu} \frac{dp}{dL} \quad (12)$$

where *u_f* is specific discharge defined as *Q* divided by discharge area, *k* is the permeability of the medium, of the fluid, and *dp/dL* is the gradient in excess pressure, it is possible to express the local permeability of a fracture (*k_f*) in terms of the local fracture aperture (*b*) as:

$$k_f = \frac{b^2}{12} \quad (13)$$

Thus, a fracture bounded by two smooth, parallel plates separated by a constant aperture will exhibit a homogenous permeability. In contrast, for non-uniform fractures, permeability is spatially variable. Equation 13 shows how fracture aperture can be treated as an analog for permeability in fractured media; thus, these two terms are used interchangeably throughout this work when appropriate. It is important to note that the fracture apertures derived from Eq. 13 and in the Hawkins et al. 2020 dataset

are a proxy of the hydraulic performance of the reservoir (i.e., hydraulic aperture), which is different from the true actual separation between the fracture surfaces (i.e., true or mechanical aperture). As such, in this study, we use the term fracture aperture to refer to the hydraulic aperture of the fracture.

Considering field-constrained fracture aperture distributions enables us to evaluate the impact of operational design considerations on thermal performance. To do this, we up-scale the permeability distribution at Altona using a simple renormalization technique by multiplying the spatial coordinates of optimized aperture distribution in Fig. 2A by a scale factor of 42.55 such that a previous well separation of 14.1 m at Altona, corresponds to a well separation length of 600 m in the upscaled model (Fig. 3). The resulting permeability distribution covers a circular area with radius of 500 m and the orientation of the fracture is such that due North is aligned with the positive y-axis in Fig. 3.

By upscaling the geometry and statistical appearance of the original rock surface, we are able to assess extraction parameters appropriate for utility-scale geothermal fields, while preserving the original spatial correlation of self-affine rock surfaces (Yavari et al. 2002). Our *local-global* up-scaling technique does not aim to represent the regional permeability surrounding the Altona Field Laboratory. Instead, it represents a synthetic, self-affine permeability distribution for a large-scale reservoir displaying a highly channelized hydrogeological behavior. This approach resembles similar methodologies employed by Glover et al. (1998), and Gómez-Hernández and Journel (1990). Nonetheless, whereas previous studies have often upscaled high resolution petrophysical and geometrical properties directly from the core- or lab-scale (i.e., centimeters) to the field scale (kilometers), our upscaling approach is based on observations at the mesoscale (tenths of meters).

With the resulting upscaled permeability distribution, we conduct a sensitivity analysis for three attributes that reflect design/operating parameters in a commercial scale setting. These attributes are: (1) mass flow rate (ranging from 10 to 40 kg·s⁻¹); (2) well

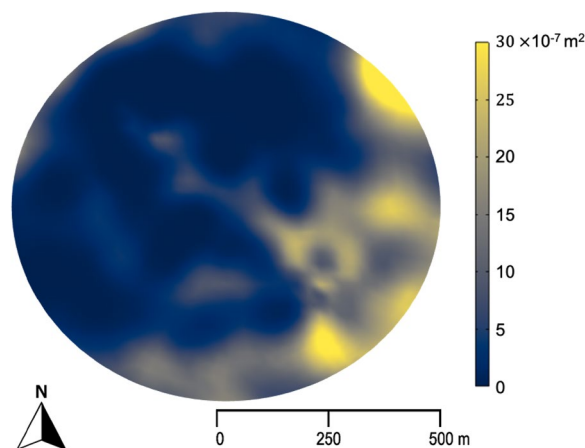


Fig. 3 Upscaled permeability distribution from Altona for a synthetic circular region of 500 m of radius. The permeability distribution was rescaled using a renormalization technique for the x and y coordinates ($dx \rightarrow k \cdot dx, dy \rightarrow k \cdot dy$) where k is 42.55. Permeability is expressed in m^2 units. Orientation of the fracture was shifted so due North is aligned with the positive y-axis

separation distance (300 to 500 m); and (3) four different flow orientations relative to North. The parameter range considered is listed in Table 2.

Model validation

To validate our modeling approach, we compare simulations with our fully numerical model against two benchmark solutions reported by Ghassemi et al. (2003) and Fox et al. (2015). Both of these studies use an alternative approach to the one implemented in our models. They solve for the heat transfer in the porous medium analytically and solve the fracture flow equations numerically. In contrast, as described in the previous section, we model both fluid flow in the fracture and in the bulk rock matrix numerically.

As shown in Fig. 4, our purely numerical COMSOL simulation results of production temperature over time closely correspond to the hybrid numerical-analytical models of both Fox et al. and Ghassemi et al. Throughout our study, we normalize temperature T for plotting and analysis purposes to a dimensionless value that is bounded between zero and 1, following equation:

$$T_{nd} = \frac{(T - T_{inj})}{(T_r - T_{inj})} \quad (14)$$

Figure 4.A compares results of our model with those of Fox et al. (2015) considering a circular fracture with a radius of 500 m, an inter-well separation distance of 600 m, and a variety of different mass flow rates. Similarly, Fig. 4B shows the comparison with the model of Ghassemi et al. (2003) for which mass flow rate is fixed at 80 kg/s but two different fracture sizes and inter-well separation distances are considered. The first simulation considers a fracture size R of 200 m whereas, in the second simulation, the fracture size is increased to 300 m. Injection and extraction wells are located at $\pm R/2$ on the x -axis in both cases. These parameters and the remaining modeling parameters for both simulations are specified in Table 1.

Results and discussion

After validating our modeling framework, we proceed to evaluate the influence of three operating conditions on the commercial-scale thermal performance of a two-well open-loop geothermal system. In particular, we vary: mass flow rate (10 to 40 $kg \cdot s^{-1}$), well separation distance (300 to 500 m), and well relative placement along four different orientations. Table 2 describes the parameters defining our 14 simulation cases. Table 3 describes the additional model parameters that remain constant among all the simulations.

Homogenous vs heterogenous permeability fields

We first compare the thermal performance results of a base case (case 0) with a homogeneous fracture aperture to a heterogeneous case, with an equivalent mass flow rate, but uses Altona's upscaled permeability distribution (case 2). For both cases, we assume a constant mass flow rate of 20 kg/s, an initial reservoir temperature of 200 °C, reinjection temperature of 50 °C, and an inter-well spacing of 500 m from West to East. At initial time, both case 0 and case 2 provide a production well thermal power of 12.5 MW_{th} .

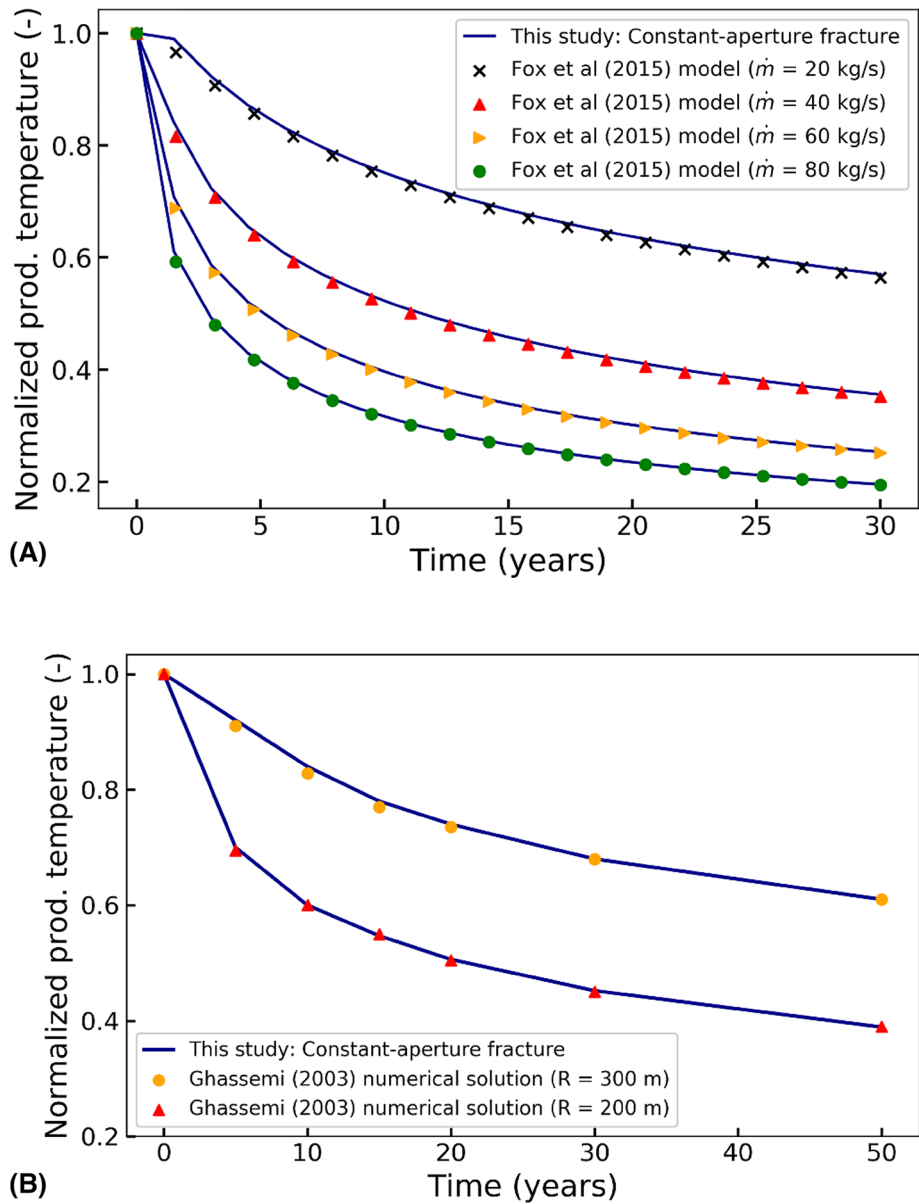


Fig. 4 Model validation results with benchmark solutions for single-fracture reservoirs displaying uniform aperture. **A** Model comparison with Fox et al. (2015). The graph shows simulations for four different mass flow rates (20, 40, 60, and 80 kg/s). **B** Model comparison with Ghassemi et al (2003). Graph shows simulations for two fracture lengths (200 and 300 m). The rest of modeling parameters for both validations are contained in Table 1

This initial thermal power production is governed by the initial reservoir temperature and equivalent injection rates. However, at the end of the 10 year heat extraction period, both case 0 and case 2 experience declines in production well temperatures from 200 °C down to 152 °C and 160 °C, respectively (Fig. 5). These temperature declines correspond to a thermal power output that drops from 12.5 MW_{th} to 8.5 and 9.2 MW_{th}, respectively. In the thermal exchange maps (Fig. 5), the regions that remain at high temperatures (in red) after one year of continuous circulation correspond to areas that did not experience fracture-matrix heat transfer during the heat extraction process. In contrast, regions

Table 1 Summary of the modeling parameters for the cross-validation with benchmark solutions

Parameter	Symbol	Values for Fox et al. (2015) validation	Values for Ghassemi et al. (2003) validation
Uniform fracture aperture	b	5 mm	5 mm
Specific heat capacity of the fluid	$C_{p,f}$	4184 J/(kg · K)	4050 J/(kg · K)
Specific heat capacity of the rock	$C_{p,r}$	1000 J/(kg · K)	1100 J/(kg · K)
Thermal conductivity of the fluid	k_f	0.6 W/(m · K)	0.6 W/(m · K)
Thermal conductivity of the rock	k_r	2.40 W/(m · K)	2.58 W/(m · K)
Dynamic viscosity of the fluid	μ	1E-3 Pa · s	1E-3 Pa · s
Fluid density	ρ_f	1000 kg/m ³	1000 kg/m ³
Rock density	ρ_r	2300 kg/m ³	2650 kg/m ³
Reinjection temperature	T_{inj}	50 °C	60 °C
Reservoir temperature	T_r	200 °C	140 °C

Values specified in the third and fourth columns correspond to values reported by Fox et al. (2015) and Ghassemi et al. (2003), respectively

Table 2 List of cases simulated

Case No	Mass flow rate, \dot{m} (kg · s ⁻¹)	Well separation distance, W_{sd} (m)	Fluid circulation direction
<i>Homogenous fracture aperture distribution</i>			
0	20	500	W–E
<i>Heterogeneous fracture aperture distribution; varying flow rates</i>			
1	10	500	W–E
2	20	500	W–E
3	40	500	W–E
<i>Heterogeneous fracture aperture distribution; varying well separation</i>			
4	20	300	W–E
5	20	400	W–E
6	20	500	W–E
7	20	300	N–S
8	20	400	N–S
9	20	500	N–S
<i>Heterogeneous fracture aperture distribution; varying well pair orientation</i>			
10	20	500	W–E
11	20	500	N–S
12	20	500	NW–SE
13	20	500	NE–SW

Case 0 represents the base case of an ideal fracture displaying constant aperture. The subsequent cases use Altona's upscaled permeability distribution. Cases 1 through 3 model the influence of mass flow rate. Cases 4 through 9 model the influence of well separation distance along the y- and x-axis, and Cases 10 through 13 evaluate the influence of the relative well placement. E, W, N, and S denote the four Cardinal points. Note that the direction of fluid circulation in Case 0 can be selected arbitrarily, since fluid circulation direction is inconsequential for a uniform permeability field

that are cold (blue) are zones in which heat extraction occurred. Thermal exchange maps for this pair and all other simulations are expressed in normalized temperature (Eq. 14).

Figure 5A exhibits ideal dipole flow along a uniformly permeable fracture, whereas the thermal exchange map in Fig. 5B is characterized by highly irregular patterns reflective of flow channeling. The creation of these irregular patterns has a direct influence on the effective heat transfer surface area and, as a result, determines the thermal performance

Table 3 Summary of the model parameters that remain constant in the 14-case sensitivity study described in Table 2

Parameter	Symbol	Values
Rock block height	H	100 m
Rock porosity	ϕ_r	0.1
Specific heat capacity of the fluid	$C_{p,f}$	4184 J/(kg·K)
Specific heat capacity of the rock	$C_{p,r}$	1000 J/(kg·K)
Thermal conductivity of the fluid	k_f	0.6 W/(m·K)
Thermal conductivity of the rock	k_r	2.4 W/(m·K)
Rock density	ρ_r	2300 kg/m ³
Reinjection temperature	T_{inj}	50 °C
Initial reservoir temperature	T_r	200 °C
Well radius	w_r	0.15 m

of a given injector-producer well pair. Whereas extreme flow channeling often results in short-circuiting and poor thermal performance, in this example the well positioning and resulting flow field results in thermal performance which slightly outperforms the idealized constant aperture fracture (Fig. 5C). As for the influence of the fracture aperture on thermal performance in the base case (i.e., case 0), the magnitude of the aperture is irrelevant since the mean fracture aperture does not influence thermal performance as long as mass flow rate is maintained (e.g., Hawkins et al. 2018). This is because the effective fluid-matrix heat transfer area is independent of the fracture aperture. However, the mean fracture aperture does affect the hydraulic performance (i.e. inter-well pressure drop) and reservoir volume.

Mass flow rate

To assess the influence of mass flow rate on thermal performance considering the extremely heterogenous aperture distribution, we specify an inter-well separation of 500 m and circulate in the west–east direction for cases with different mass flow rates. Figure 6 shows thermal performance results over 10 years of continuous heat extraction for mass flow rates of 10, 20, and 40 kg/s (Cases 1, 2, and 3, respectively). The y-axis to the left reflects the normalized production temperature (Eq. 14), whereas the label on the right reflects the absolute production temperature in degrees Celsius, where 200 °C is the original reservoir temperature (i.e., $T_{nd} = 1$) and 50 °C corresponds to the reinjection temperature ($T_{nd} = 0$).

The impact of varying mass flow rates reveals, as expected, that higher production temperatures result when lower mass flow rates are specified. Figure 6 might give the reader the impression that low mass rates lead to superior thermal performance considering that for case 1, 2, and 3, the resulting percent decline in production well temperatures after 10 years are 9%, 27%, and 52%, respectively. However, from the perspective of thermal power produced (Fig. 7), the highest mass flow rate we considered (case 3, 40 kg/s) overcomes the effect of resulting in a lower production temperature and yields the greatest thermal power production (25 MW_{th}) owing to its considerably higher volumetric throughput. After 10 years of heat extraction, case 1, 2, and 3 yield thermal power outputs of roughly 6, 9, and 12 MW_{th}, respectively. The 10 kg/s circumstance (case 1) shows a nearly constant thermal power output

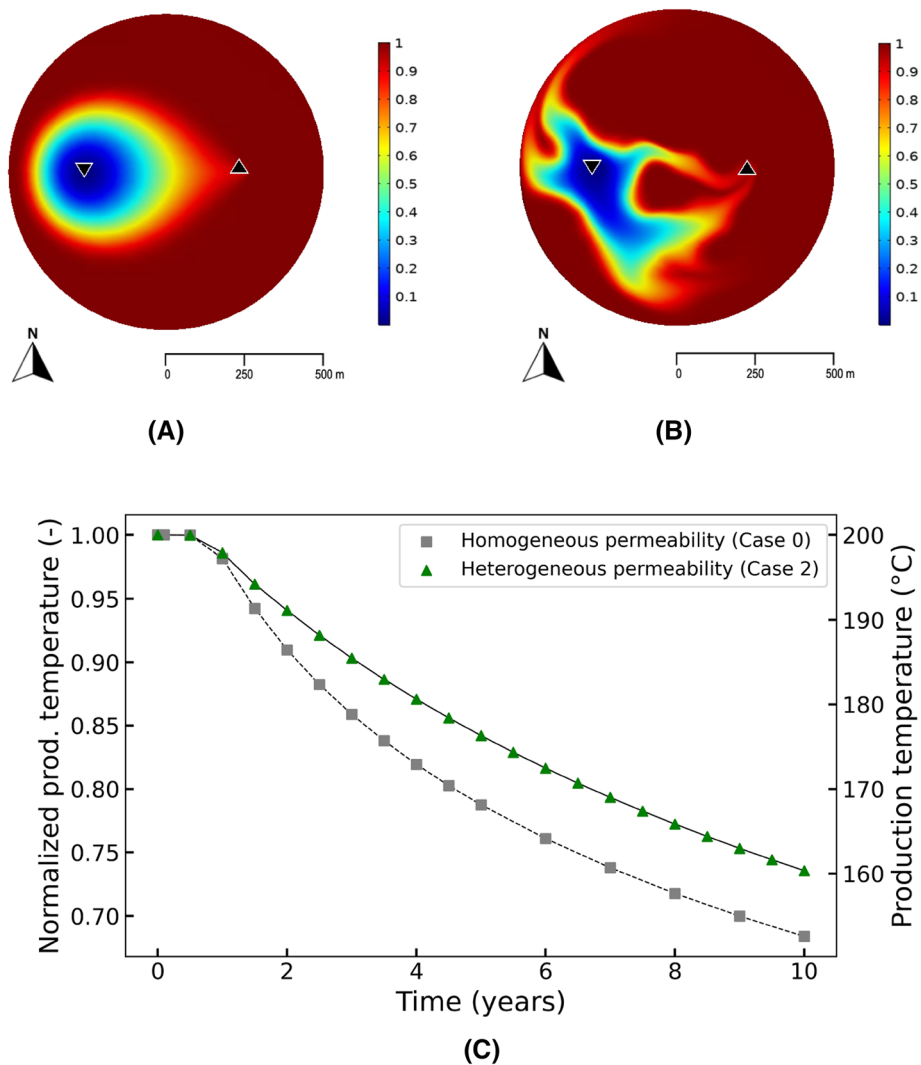


Fig. 5 **A** and **B** Thermal exchange maps after 1 year of geothermal extraction, for an injection well in left sector (down-facing triangle) to an extraction well in the right sector (up-facing triangle). Case 0, on the left depicts the dipole model that considers a constant permeability. Case 1, on the right, depicts the geothermal extraction that occurs for the up-scaled permeability distribution at Altona (Fig. 3C) Thermal drawdown curves over a 10 year period. Both simulations consider the following parameters: mass flow rate of $2020 \text{ kg} \cdot \text{s}^{-1}$, reservoir temperature of $200 \text{ }^\circ\text{C}$, reinjection temperature of $50 \text{ }^\circ\text{C}$, and an inter-well spacing of 500 m from West to East

throughout the lifetime whereas the 20 kg/s circumstance (case 2) shows a moderate decline from roughly 13 to 9 MW_{th} . Meanwhile, the 40 kg/s circumstance (case 3) yields the largest decline in thermal power output (from roughly 25 to $12 \text{ MW}_{\text{th}}$), but remains the superior case in terms of the cumulative thermal power output. In geothermal extraction, optimum mass flow rates are those that ensure long-term generation of high-temperature production fluids while still delivering sufficient power output for a specific need. For instance, according to Clauser (2006), flow rates and production temperatures in excess of 50 kg/s and $150 \text{ }^\circ\text{C}$, respectively, are considered optimal for the economic generation of electrical energy. However, even higher

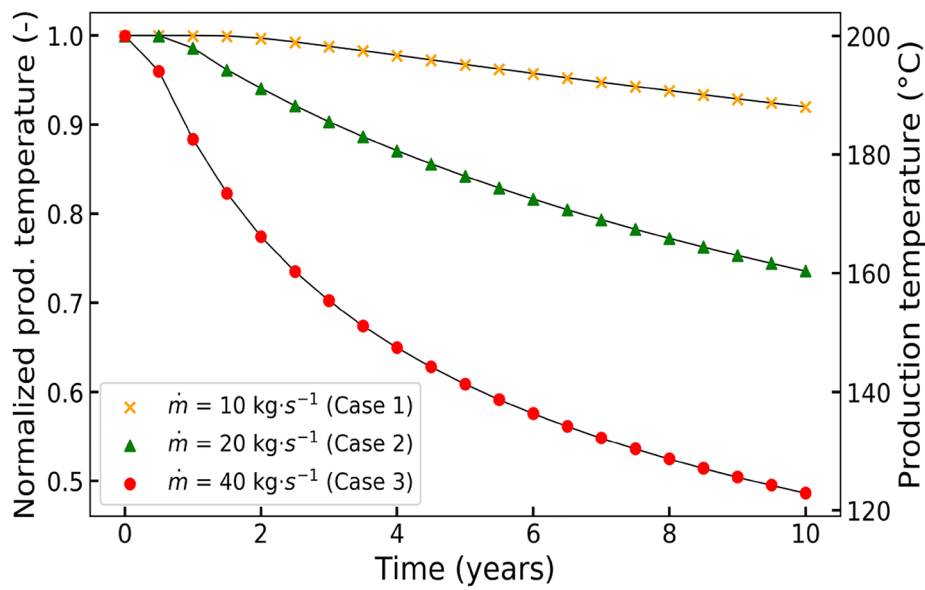


Fig. 6 Impact of mass flow rate on the production temperatures at the extraction well. Fluid circulation occurred from West to East and the inter-well separation distance was fixed at 500 m

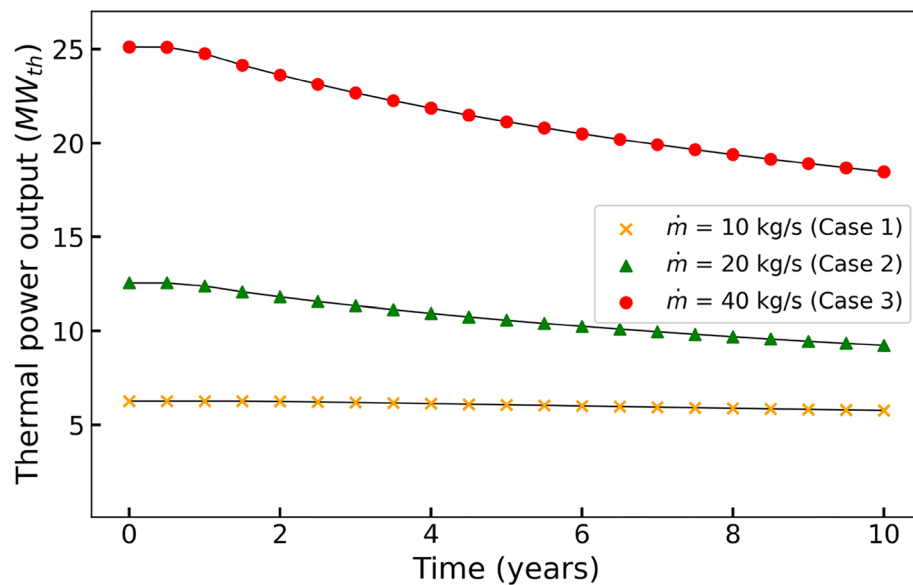


Fig. 7 Impact of mass flow rate on thermal power generation. Thermal power generation was calculated using $P = \dot{m}C_p\Delta T$ where P is thermal power, C_p is the specific heat capacity of the fluid and ΔT is the difference between the temperature of the working fluid being produced and the reinjection temperature

production temperatures may still be uneconomical if they drop considerably below what was originally intended.

Reducing the mass flow rate leads to smaller temperature drops by the end of the ten-year period of evaluation, but the corresponding thermal power output suffers as a result. Case 1, for instance, considered a mass flow rate of 10 kg/s which limited production well temperature drop to 13 °C, but the corresponding thermal power

output is just 5.8 to 6.3 MW_{th}. In contrast, increasing the mass flow rate leads to greater temperature drops, but the corresponding thermal power output begins at 25 MW_{th} and remains above 12 MW_{th} for the entire 10 year heat extraction period.

Well separation distance

After evaluating the influence of mass flow rate, cases 4 through 9 evaluate the influence of varying the inter-well separation distance between 300 and 500 m along two perpendicular directions, specified at a mass flow rate of 20 kg/s. In general, it is expected that larger separation distances between injection and production wells imply larger subsurface reservoirs, which in turn promote larger surface area and longer sustained production temperatures. Figures 8, 9 show the thermal exchange maps and the thermal drawdown curves resulting from varying the well separation distance for the permeability distribution shown in Fig. 3. As expected, varying the well spacing along either the W-E or the N-S direction appear to increase the heat exchange area thus respecting the prediction of thermal performance improvement mentioned above (Fig. 9). However, increases in well spacing along the y-axis appear to have a lesser influence compared to the same variations along the x-axis (Fig. 8). Varying the well separation distance along the x-axis (E-W) leads to a considerably higher variability in thermal performance, yielding final production temperatures in the range of 98 to 160 °C. However, conducting the same variation along the y-axis (N-S) yields a production temperature range of 122 to 138 °C at the end of the 10 year period. As such, the relationship between well spacing and thermal power production in heterogeneous fields is not linear because the effective reservoir area available for heat extraction does not scale proportionally. Thus, under such conditions and in contrast to homogenous reservoirs, thermal performance improvements do not scale linearly either.

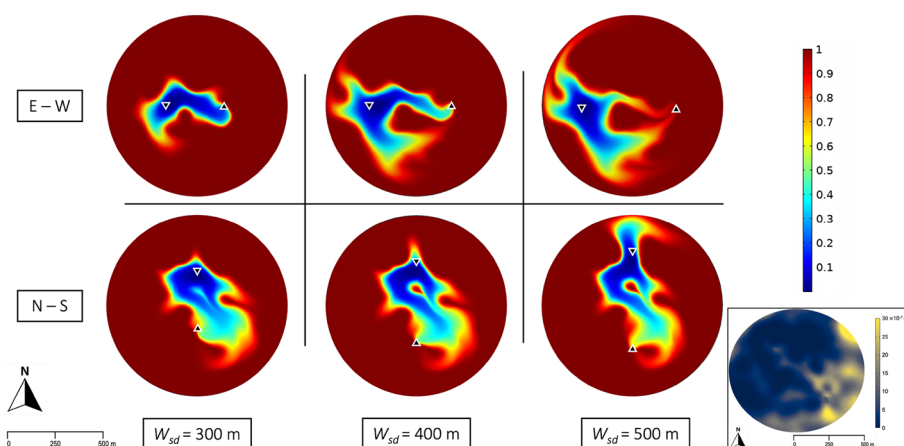


Fig. 8 Temporal evolution of the thermal front advance for cases 4 through 9. Interwell separation distance varies from 300 to 500 m along the x-axis (first row) and the y-axis (second row). For the set of panels in the first row, fluid circulation occurs from an injection well in the western sector to an extraction well in the eastern sector. Fluid circulation for all panels in the second row occurs from an injection well in the northern sector to a production well in the southern sector. T_{nd} represents the reservoir’s dimensionless temperature and W_{sd} represents the inter-well spacing. Columns depict thermal exchange state after 1 year of continuous operation. Image on the bottom right corner represents the up-scaled permeability distribution

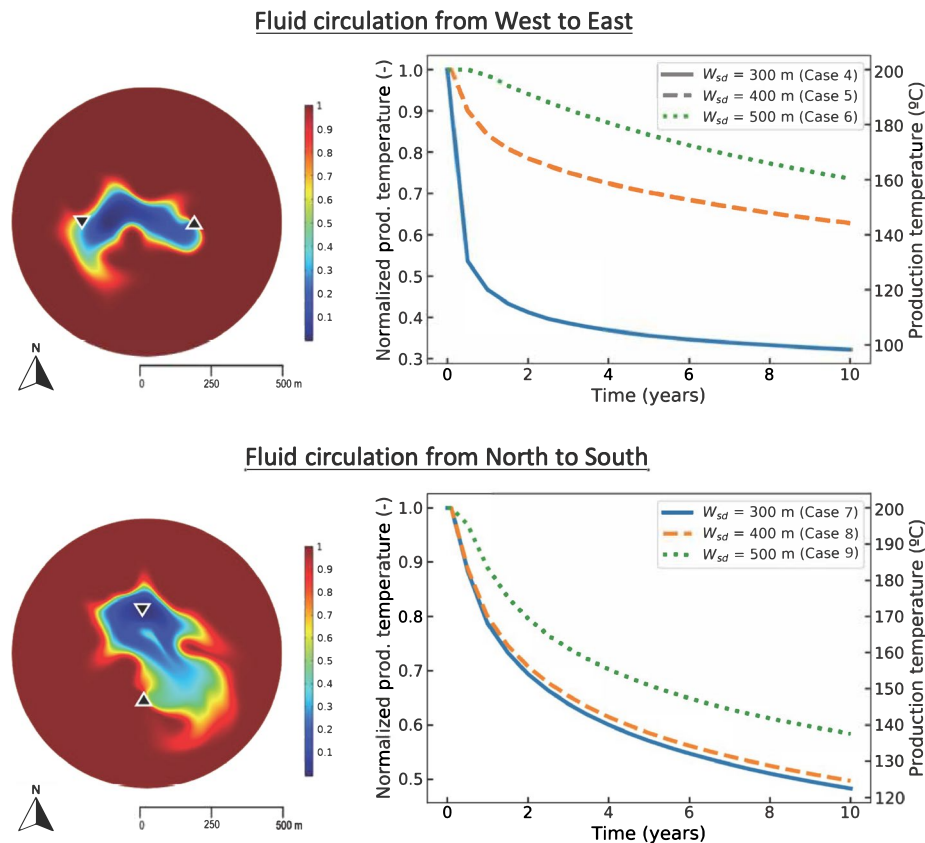


Fig. 9 Impact of well separation distance, along two arbitrary directions, on thermal performance. Diagrams in the left column show the thermal exchange map after 1 year of operation with well separation distance of 300 m in both cases. Simulated thermal drawdown plots in the second column depict the production temperature evolution for 10 years, for cases of 300 m, 400 m, and 500 m distances between the injection and production wells

It is worth noting that, varying exclusively well separation distance, leaving all other extraction parameters unchanged, the West to East fluid circulation generates both the best-case scenario and worst-case scenario for power generation—for all cases considered. While the results of variations along the N-S axis were all located in a relatively narrow range in terms of thermal power generation. This non-linear relationship constitutes a non-intuitive dependence of heat production on fluid circulation orientation relative to the flow channel that is explored in the next subsection.

Relative wellbore positioning

The findings of the well separation distance variations described above are indicative of the influence of the relative placement of wellbores in channelized fields. Thus, two final circumstances are considered to evaluate the influence of extracting heat in the north-west-southeast orientation (case 12) and in the northeast-southwest orientation (case 13). For both cases, the well separation is specified to be 500 m and the mass flow rate is 20 kg/s. For cases 12 and 13, production well temperatures fell from 200 °C to 99 and 153 °C, respectively (Fig. 10). These temperature drops correspond to thermal power output falling from 12.6 MW_{th} to 4.1 and 8.6 MW_{th}, respectively. For comparison,

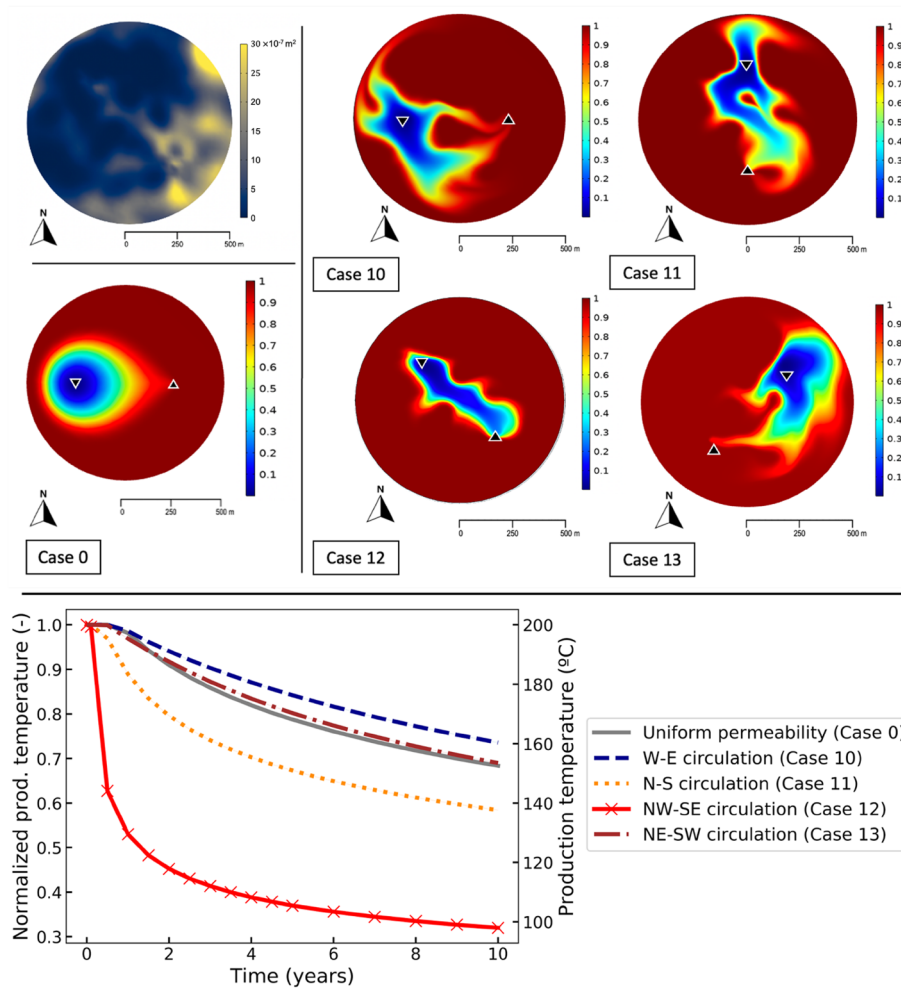


Fig. 10 Up-scaled permeability distribution on the upper left-hand side of the figure alongside simulated thermal exchange maps for Case 0, on the bottom left-hand side, and Cases 10 through 13, on the right. Below, thermal drawdown curves for all cases considering a continuous mass flow rate of $20 \text{ kg} \cdot \text{s}^{-1}$ and a well separation distance of 500 m over 10 years of geothermal extraction. Thermal exchange maps depict the advancement of the thermal front after 1 year of operation

Fig. 10 also shows the thermal performance results of geothermal energy extraction along 4 different directions in a heterogeneous field (cases 10 through 13) against the base case with uniform permeability (case 0). We observe how fluid circulation from West to East (case 10) and fluid circulation from Northeast to Southwest (case 13) show marginal improvements relative to the thermal performance of the base case, whereas the production temperatures for cases in which the fluid circulation occurs from North to South (case 11) and Northwest to Southeast (case 12) considerably decreases due to extreme flow channeling.

These results illustrate the importance of fluid circulation orientation in heterogeneous reservoirs. As anticipated, we observe that certain circulation orientations are more susceptible to thermal performance variability, resulting in greater uncertainty in reservoir performance. For instance, in the north–south orientation, we observe minimum and maximum temperature drops of 41% and 52% respectively. Whereas,

in stark contrast, the west–east orientations exhibited a much higher variability with minimum and maximum temperature drops of 26% and 67% respectively.

Furthermore, thermal performance is critically impacted when fluid circulation occurs in parallel to the orientation of the main channel (Case 12; Fig. 10). Although logically overlooked when modeling idealized fractures, the orientation in which the fluids are circulated in rough fractures has a considerable impact in determining the fluid flow distribution and thermal performance.

Summary and conclusions

Overall, our results illustrate the effects that an extremely channelized heterogeneous fracture system, in this case informed by real-world meso-scale observations, can have on geothermal performance. Although such a reservoir is susceptible to short-circuiting and poor thermal performance, our results reveal that the reservoir also has the potential to perform better than expected considering a constant aperture/uniform permeability fracture depending on well separation and positioning of the wells relative to the flow channel. As expected, we find that short-circuiting is worst when the injector and/or producer are located directly within and/or when their relative placement is aligned parallel to the high permeability channel. These scenarios result in rapid thermal drawdown. However, there are tradeoffs between trying to maintain production temperature and sustained thermal power production. As long as the production temperature remains within working range, it may be possible to maintain large power production for long periods using higher flow rates despite the greater negative effect on production temperature.

Our results also illustrate how wells positioned perpendicular or obliquely to the main permeability channel can result in flow paths covering large amounts of surface area and less thermal drawdown than expected considering a constant aperture fracture. These scenarios provide guidance for operators who may find themselves in an uneconomic short-circuiting system due to extreme flow channeling. Before abandoning the reservoir completely, our results suggest that investment in characterization of the permeability field using tracers and other observables using what wells are available may be worthwhile. As demonstrated here, characterization of the permeability field can help elucidate if and where an additional well could be positioned to increase the heat exchange surface area and enable flow path directions that are oblique to main permeable channels such that longer residence time and heat exchange is maintained. Overall, this work illustrates why further investment in characterizing reservoirs with such extreme flow channels, even if they are not further developed, can help in developing best practices for mitigating their effects or for optimizing production, potentially with a new well, in a field whenever extreme short-circuiting is encountered.

Acknowledgements

The authors would like to thank Jefferson Tester and Terry Jordan for providing valuable insights on geothermal systems engineering and reservoir characterization, and Ivan Purwamaska for providing help with COMSOL modeling.

Author contributions

NRJ: Investigation, Formal analysis, Software, Manuscript writing—review and editing. AJH: Supervision, Funding, Writing—review and editing. PMF: Supervision, Funding, Writing—review and editing. All authors read and approved the final manuscript.

Funding

This work was partially funded by the U.S. Department of Energy-funded project for deep direct-use of geothermal energy at Cornell University (Award Number DE-EE0008103) and by the U.S. Department of Energy-funded project for Innovative Methods to Control Hydraulic Properties of Enhanced Geothermal Systems (Award Number DE-FOA-0002498).

Availability of data and materials

The datasets used and/or generated during the current study are available from the corresponding author on reasonable request.

Declarations

Competing interests

The authors declare that they have no known competing financial interests or personal relationships that could have influenced the work reported in this article.

Received: 15 March 2022 Accepted: 26 June 2023

Published online: 22 July 2023

References

- Brown SR. Fluid flow through rock joints: the effect of surface roughness. *J Geophys Res.* 1987;92:1337–47. <https://doi.org/10.1029/JB092iB02p01337>.
- Bundschuh J, César Suárez A, M. Introduction to the numerical modeling of groundwater and geothermal systems in introduction to the numerical modeling of groundwater and geothermal systems. Boca Raton: CRC Press; 2010. <https://doi.org/10.1201/b10499>.
- Chandrasekharam D, Bundschuh J. Low-enthalpy geothermal resources for power generation energy sources, part a: recovery. *Util Environ Effects.* 2008;31(1):98. <https://doi.org/10.1080/15567030802557058>.
- Clauser, C. Geothermal energy. *Adv Mater Technol.* 2006.
- Comsol. Subsurface flow module. In COMSOL multiphysics reference manual. 2019. https://doc.comsol.com/5.5/doc/com.comsol.help.comsol/COMSOL_ReferenceManual.pdf
- Corbett PWM, Jensen JL, Sorbie KS. A review of up-scaling and cross-scaling issues in core and log data interpretation and prediction. *Geol Soc Spec Pub.* 1998;136:9–16. <https://doi.org/10.1144/GSL.SP.1998.136.01.02>.
- Farmer CL. Upscaling: a review. *Int J Numer Meth Fluids.* 2002;40(1–2):63–78. <https://doi.org/10.1002/flid.267>.
- Fox DB, Koch DL, Tester JW. The effect of spatial aperture variations on the thermal performance of discretely fractured geothermal reservoirs. *Geother Energy.* 2015. <https://doi.org/10.1186/s40517-015-0039-z>.
- Ghassemi A, Tarasovs S, Cheng AHD. An integral equation solution for three-dimensional heat extraction from planar fracture in hot dry rock. *Int J Numer Anal Meth Geomech.* 2003;27(12):989–1004. <https://doi.org/10.1002/nag.308>.
- Ghassemi A, Tarasovs S, Cheng AHD. Integral equation solution of heat extraction-induced thermal stress in enhanced geothermal reservoirs. *Int J Numer Anal Meth Geomech.* 2005;29(8):829–44. <https://doi.org/10.1002/nag.440>.
- Glover PWJ, Matsuki K, Hikima R, Hayashi K. Fluid flow in synthetic rough fractures and application to the Hachimantai geothermal hot dry rock test site. *J Geophys Res Solid Earth.* 1998;103(5):9621–35. <https://doi.org/10.1029/97jb01613>.
- Gomez-Hernandez, J. J., and A. G. Journal. "Stochastic characterization of grid-block permeabilities: from point values to block tensors." ECMOR II-2nd European Conference on the Mathematics of Oil Recovery. European Association of Geoscientists and Engineers. 1990.
- Guo B, Fu P, Hao Y, Peters CA, Carrigan CR. Thermal drawdown-induced flow channeling in a single fracture in EGS. *Geothermics.* 2016;61:46–62. <https://doi.org/10.1016/j.geothermics.2016.01.004>.
- Hawkins AJ. Reactive tracers for characterizing fractured geothermal reservoirs. Ithaca: Cornell University; 2017.
- Hawkins AJ, Becker MW, Tsofilas GP. Evaluation of inert tracers in a bedrock fracture using ground penetrating radar and thermal sensors. *Geothermics.* 2017a;67:86–94. <https://doi.org/10.1016/j.geothermics.2017.01.006>.
- Hawkins AJ, Fox DB, Becker MW, Tester JW. Measurement and simulation of heat exchange in fractured bedrock using inert and thermally degrading tracers. *Water Resour Res.* 2017b;5(3):2–2. <https://doi.org/10.1111/j.1752-1688.1969.tb04897.x>.
- Hawkins AJ, Becker MW, Tester JW. Inert and adsorptive tracer tests for field measurement of flow-wetted surface area. *Water Resour Res.* 2018;54(8):5341–58. <https://doi.org/10.1029/2017WR021910>.
- Hawkins AJ, Fox DB, Koch DL, Becker MW, Tester JW. Predictive inverse model for advective heat transfer in a short-circuited fracture: dimensional analysis, machine learning, and field demonstration. *Water Resour Res.* 2020;56(11):1–20. <https://doi.org/10.1029/2020WR027065>.
- Hui MHR, Karimi-Fard M, Mallison B, Durlofsky LJ. A general modeling framework for simulating complex recovery processes in fractured reservoirs at different resolutions. *SPE J.* 2018;23(2):598–613. <https://doi.org/10.2118/182621-pa>.
- Kolditz O, Clauser C. Numerical simulation of flow and heat transfer in fractured crystalline rocks application to the hot dry rock site in rosemanowes (UK). *Geothermics.* 1998;27:1–23.
- Lu S. Global review of enhanced geothermal system (EGS). *Renewable Sustain Energy Rev.* 2018;81:2902.
- Murphy HD, Tester JW, Grigsby CO, Potter RM. Energy extraction from fractured geothermal reservoirs in low-permeability crystalline rock. *J Geophys Res.* 1981;86(B8):7145–58. <https://doi.org/10.1029/JB086iB08p07145>.
- National Research Council. Rock fractures and fluid flow contemporary understanding and applications. Elsevier: The National Academies Press; 1996.

- Neuvillle A, Toussaint R, Schmittbuhl J. Fracture roughness and thermal exchange: a case study at Soultz-sous-Forêts. *Comptes Rendus Geosci.* 2010;342(7–8):616–25. <https://doi.org/10.1016/j.crte.2009.03.006>.
- Olcott, P. Ground water atlas of the United States. 1995.
- Pandey SN, Vishal V. Sensitivity analysis of coupled processes and parameters on the performance of enhanced geothermal systems. *Sci Rep.* 2017. <https://doi.org/10.1038/S41598-017-14273-4>.
- Pyrak-Nolte LJ, Braverman W, Nolte NJ, et al. Probing complex geophysical geometries with chattering dust. *Nat Commun.* 2020;11:5282. <https://doi.org/10.1038/s41467-020-19087-z>.
- Rayburn JA, Knuepfer PLK, Franz DA. A series of large, late wisconsinan meltwater floods through the Champlain and Hudson valleys, New York State, USA. *Quatern Sci Rev.* 2005;24:2410–9. <https://doi.org/10.1016/j.quascirev.2005.02.010>.
- Sicking C, Malin P. Fracture seismic: mapping subsurface connectivity. *Geosciences.* 2019;9:508. <https://doi.org/10.3390/geosciences9120508>.
- Tsang, C. and Neretnieks, I. Flow channeling in heterogeneous fractured rocks. *reviews of geophysics.* 1997. <https://escho.larship.org/uc/item/8zw551hg>
- Watanabe N, Wang W, McDermott CI, Taniguchi T, Kolditz O. Uncertainty analysis of thermo-hydro-mechanical coupled processes in heterogeneous porous media. *Comput Mech.* 2010;45(4):263–80. <https://doi.org/10.1007/s00466-009-0445-9>.
- Witherspoon PA, Wang JSY, Iwai K, Gale JE. Validity of cubic law for fluid flow in a deformable rock fracture. *Water Resour Res.* 1980;16(6):1016–24.
- Yavari A, Sarkani S, Moyer ET. The mechanics of self-similar and self-affine fractal cracks. *Int J Fract.* 2002;114(1):1–27. <https://doi.org/10.1023/A:1014878112730>.
- Zhao Z, Dou Z, Liu G, Chen S, Tan X. Equivalent flow channel model for doublets in heterogeneous porous geothermal reservoirs. *Renew Energy.* 2021;172:100–11. <https://doi.org/10.1016/j.renene.2021.03.024>.
- Zimmerman RW, Bodvarsson GS, Bodvarsson GS. Hydraulic Conductivity of rock fractures. *Trans Porous Media.* 1996. <https://doi.org/10.1007/BF00145263>.

Publisher's Note

Springer Nature remains neutral with regard to jurisdictional claims in published maps and institutional affiliations.

Submit your manuscript to a SpringerOpen[®] journal and benefit from:

- ▶ Convenient online submission
- ▶ Rigorous peer review
- ▶ Open access: articles freely available online
- ▶ High visibility within the field
- ▶ Retaining the copyright to your article

Submit your next manuscript at ▶ [springeropen.com](https://www.springeropen.com)
